RSC Advances

ROYAL SOCIETY OF CHEMISTRY

www.rsc.org/advances

In Situ Preparation of Cobalt Doped ZnO@C/CNT Composites by Pyrolysis of Cobalt Doped MOF for High Performance Lithium Ion Battery

Hongyun Yue[*abc], *Zhenpu Shi*[a], *Qiuxian Wang*[a], *Ting du*[a], *Yanmin Ding*[a], *Jun Zhang*[a], *Ningning Huo*[a] *and Shuting Yang*[*abc]

a School of Chemistry and Chemical Engineering, Henan Normal University, Xinxiang, Henan 453007, China.

b Engineering Technology Research Center of Motive Power and Key Materials, Xinxiang, Henan 453007, China

c Collaborative Innovation Center of Henan Province for Motive Power and Key Materials, Xinxiang, Henan 453007, China

*Corresponding Author E-mail: yuehongyun@foxmail.com; shutingyang@foxmail.com; Fax: (+86)-373-3326439; Tel: (+86)-373-3326439

KEYWORDS. zinc oxide; metal organic frameworks; carbon nanotube; cobalt doping; anode material; Lithium ion batteries

ABSTRACT. Co doped ZnO embedded within carbon/carbon nanotube composites (CZO@C/CNT) was in situ prepared during the calcination of Co-MOF-105 at 600 °C. The lower crystallinity demonstrated a weaker binding force in Co-MOF-105, which made it possible that the Co ion breakaway from the crystal and reduced to metal Co during the pyrolysis process. The formation of CNTs was catalyzed by metal Co and the carbon source was terephthalic acid which played as the organic linker in MOF. Moreover, the sp^2 hybridization during which the carbon atoms were in terephthalic acid decreased the energy barrier during the growth of CNTs. From TEM and SEM observation, the CNTs were interspersed in the material and connected the

CZO@C nanoparticles together, which made the electron transfer easier. The other advantages of Co doping were enhancing the conductivity of ZnO and increasing the graphitization degree of the carbon on the surface of CZO@C nanoparticles. When the CZO@C/CNT composite was used as anode material for lithium ion battery , an enhanced electrochemical performance of 758 mA h g^{-1} after 100 cycles at the current density of 100 mA g^{-1} was obtained.

1. INTRODUCTION

Environment pollution and the exhaustion of fossil fuel are two major problems facing to human being. An effective way is to replace traditional motor vehicle by electric vehicle (EV). However, the development of EV is limited by the high efficiency, high security and long cycle life of batteries . [1-4] Lithium ion batteriy (LIB) is a promising candidate due to its high energy density and long cycle life. So that, developing novel anode materials to meet the critical demand of EVs is a popular topic. [5-7] As an anode material, ZnO has higher theoretical lithium storage capacity (987 mA h g^{-1}) than traditional graphite (372 mA h g^{-1}) and higher lithium ion diffusion coefficient compared to other transition metal oxides. [8, 9] In addition, ZnO is cheap and nontoxic. [10] While, similar to other metal oxides, ZnO undergoes volume expansion and poor electrical conductivity during cycling which results in pulverization of the electrodes and limited rate performance. [11, 12] The present solutions to overcome the disadvantages above consist of carbon coating, [13] nanoparticle preparing, [14] metal doping[15] and oxides compositing. [16] The doping and compositing conductive carbon materials, [12, 17] such as combining carbon nanotubes (CNTs)[18] with metal oxide, also attracted many researchers' attention in recent years.

Metal−organic frameworks (MOFs) are a class of rapidly growing adsorbent materials that have high surface area with high porosities. [19, 20] MOFs have been studied in many fields owing to their excellent properties, such as gas storage and separation, [21] sensing or recognition, [22]

catalysis, [23] electrochemistry, [24] and so on. Presently, the application of MOFs in electrochemistry is still in its infancy, and they are most commonly used as precursors during the synthesis of nano metal oxides or nanoporous carbon. [25] The metal centers and functional linkers of MOF are ordered arrangement at long range. The ultra small particles of metal oxide which coated with carbon can be prepared by simply pyrolysis of MOFs under inert atmosphere. [26] Metal ions can be easily absorbed by MOFs, which provide a simple way to prepare doped metal oxides. [27] The porous carbon-coated ZnO quantum dots (QDs) derived from MOF exhibits nearly 100% capacity retention after 50 cycles. [28] Zhang et al, developed a route to directly grow ZnO@ZnO QDs/C core–shell nanorod arrays (NRAs) on flexible carbon cloth substrate, which can deliver a capacity retention of 699 mA h g^{-1} after 100 cycles at 500 mA g^{-1}. [29] Our previous work reported cobalt doped ZnO@C (CZO@C) exhibitted a capacity of 525 mA h g^{-1} up to the 50^{th} cycle at a current density of 100 mA g^{-1}. [30]

In this work, the cobalt (Co) doped ZnO@C/CNTs (CZO@C/CNTs) composites was synthesized by pyrolysis of cobalt doped MOF (Co-MOF). At the best doping amount of 2%, [30] the conductivity of ZnO was enhanced and the graphitization degree of the carbon on the surface of CZO@C nanoparticles was increased, which were proved by our previous work. Although an enhanced performance was obtained in our previous work, the synthesis condition was hard to control for the pyrolysis of MOF by immediate cooling without holding at maximum temperature. In present work, the calcination condition was easy to control. Additionally, the binding force between Co and organic linker was weaker when the reaction temperature was 105 °C than that of 120°C. Therefore, a small amount of Co ion was reduced to metal Co during the pyrolysis and played as catalyst for the growth of CNTs. The CNTs were interspersed in parent carbon which embedded with ZnO nanoparticles and it was likely that the CNTs were

conductive wires which linked the ZnO@C composites together. All of the three advantages of Co doping made the electron transfer easier in the material. When the CZO@C/CNT composite was used as anode material for lithium ion battery , an enhanced electrochemical performance of 758 mA h g^{-1} after 100 cycles at the current density of 100 mA g^{-1} was obtained.

2. EXPERIMENTAL SECTION

Materials Synthesis. Zinc nitrate hexahydrate (6.0 mmol) and terephthalic acid (2.0 mmol) were dissolved in 60 mL N,N-Dimethylformamide (DMF) in an autoclave. The reaction mixture was heated and maintained at 105 °C in an oven to yield cubic crystals of MOF-5. Cobalt nitrate hexahydrate (0.6 mmol) was added into the reaction system after the autoclaves was cooled to room temperature. The mixture was stirred for 24 h in a sealed surrounding and the reaction vessels were then kept at 105 °C for 24 h to yield Co-MOF-105 crystals. The obtained samples were washed repeatedly with ethanol and then dried in a vacuum oven at 60 °C. The Co-MOF-120 was prepared as a contrast at the reaction temperature of 120 °C.

For the synthesis of CZO@C/CNTs composite, the Co-MOF-105 was heat-treated at 600 °C for 2 h in nitrogen atmosphere with a heating rate of 5 °C min^{-1}. As contrast, the ZnO@C and CZO@C composites were synthesized by pyrolysis of MOF-5 and Co-MOF-120 at 600°C for 2 h in nitrogen atmosphere.

Materials Characterization. Transmission electron microscopy (TEM, JOEL, JEM-2100), and field emission scanning electronic microscopy (FESEM, Zeiss, JSM-6700F) were used to identify the morphological structures of the obtained samples. X-ray diffraction (XRD) was carried out on a D8 Advance (Bruker) diffractometer using Ni-filtered Cu Kα radiation (λ = 0.154184 nm). The powder samples were scanned from 10° to 80° under the operation condition of 40 kV and 40 mA. X-ray photoelectron spectroscopy (XPS, PHI 5700 ESCA) analysis was

performed using monochromated Al Kα radiation (hν = 1486.6 eV) to detect the existing state of the elements. Raman scattering measurements (Jobin Yvon HR800, HORIBA) were performed in a backscattering geometry at room temperature with a 514.5 nm line of an Ar-ion laser measure the graphitization degree of the carbon in the as synthesized composites. The specific surface area and pore size distribution were measured by the Brunauer-Emmet-Teller method (BET, Tristar-II 3020, Micromeritics).

Electrochemical Measurements. For the electrochemical evaluation of ZnO@C, CZO@C and CZO@C/CNT, the test electrodes consisted of the active powder material (60 wt%), conductive carbon black (20 wt%) as a conductor, and poly (vinylidene fluoride) (PVDF, 20 wt%) dissolved in N-methyl pyrrolidinone (NMP) as a binder. Each component was mixed well to form slurry coating on a copper foil substrate. The active material loading in each disk was ~1.7 mg, corresponding to ~1.5 mg cm^{-2}. Laboratory made, CR2032 type coin cells were assembled in an Ar-filled glove-box using a Celgard 2400 as the separator, Li foil as the counter and reference electrodes, and 1 M $LiPF_6$ in ethylene carbonate (EC) – Dimethyl carbonate (DMC) (1:1 volume) as the electrolyte. The coin cells were test between 0.01 and 3.0 V (vs. Li/Li^+) at current density of 100 mA g^{-1} using a program controlled battery test instrument (LAND CT2001A, China). The gravimetric capacity was calculated with respect to all active elements (ZnO and C). The electrochemical impedance spectra (EIS) were conducted with a Solartron SI1287+SI1260 potentiometer at 25 °C with the frequency ranging from 100 kHz to 0.1 Hz.

3. RESULTS AND DISCUSSIONS

The TEM images of CZO@C/CNTs composites was shown in Figure 1a. A large number of CNTs were found in the CZO@C/CNTs composites and there was no CNTs in ZnO@C and CZO@C composites (Figure S1a and b in the SI). Moreover, The CNTs were interspersed within

composites (Figure 1b). The CNTs were multi walled carbon nanotubes (MWCNTs) with a thickness of about 10 nm (Figure 1c) and a diameter ranging from 20 to 60 nm. Additionally, the CNTs were connected with the carbon layer of (CZO). The HRTEM image of CZO@C/CNTs was shown in Figure 1d. The interplanar spacing measured from the image of 0.284 nm was belonged to the (100) plane of ZnO (JCPDS card No. 89-7102) and the value of 0.336 nm was belonged to the (002) plane of carbon (JCPDS card No. 75-0444). It was clear that the ZnO was covered by amorphous carbon and connected with the CNTs. The endpoint of the CNTs was also observed by HRTEM (Figure 1e and 1f). In this work, a small amount of Co ion was reduced to metal Co during the pyrolysis and played as catalyst for the growth of CNTs. The nanoparticles at the endpoint of CNTs were consisted of Co element (Figure S2) and the interplanar spacing was about 0.206 nm which belonged to the (002) plane of Co (JCPDS card No. 89-7373) in Figure1f. The carbon source was terephthalic acid which played as organic linker in MOF. Moreover, the sp^2 hybridization during which carbon atoms were in terephthalic acid decreased the energy barrier during the CNTs growth.

The SEM images of as synthesized MOFs and ZnO based materials were shown in Figure 2. All the MOFs including MOF-5, Co-MOF-120 (Figure 2a) and Co-MOF-105 (Figure 2b) exhibited well defined cube morphology. Additionally, the surface of the MOF which grew at 120 °C (Figure S3a) was smoother than that at 105 °C (Figure S3b). After calcination, the cube morphology which composed of nanoparticles was retained (Figure S4a and b). Obviously, the primary nanoparticles of CZO@C and CZO@C/CNT had similar diameter of about 20 nm (Figure 2c and d). In addition, the smoother surface of Co-MOF-120 resulted in the nanoparticles closer packing of CZO@C. The CZO@C/CNT presented porous structures with CNTs interspersed in the secondary particles. The porous structures made it more convenient for the

contacting of CZO@C contact and electrolyte and the conductive CNTs connected the CZO@C nanoparticles together which made the electron transfer more easier. The two advantages mentioned above could enhance the electrochemical performance to a great extent.

The XRD patterns of as synthesized Co-MOFs were shown in Figure 3a. Both Co-MOF-105 and Co-MOF-120 exhibited similar peak position with previously reported values of MOF-5s. There was no new peak appeared and no peak shift in the pattern of Co-MOFs compared with reported MOF-5. [31] Obviously, the binary metal based MOF was formed (Figure 3a). The difference between Co-MOF-105 and Co-MOF-120 was the degree of crystallization. The lower reaction temperature resulted in a lower degree of crystallization. Combined with the SEM images, it was confirmed that more crystal defects were formed in Co-MOF-105. The lower crystallinity demonstrated a weaker binding force in Co-MOF-105, which made it possible that the Co ion breakaway from the crystal and reduced to metal Co during the pyrolysis process. The major calcined product of MOF-5 in N_2 atmosphere was carbon coated wurtzite ZnO (JCPDS card No. 89-7102) (Figure 3b). The peaks of CZO@C and CZO@C/CNT were a little shift to the low angle region and there was no new peak appeared which indicated that the Co was doped in ZnO by interstitial. The inset was the enlarged view of the ZnO based materials between 20° and 30°. The unconspicuous peak at 26° in CZO@C/CNT belonged to diffraction peak of CNTs (Figure 3b inset).

The Raman shift of the as synthesized ZnO@C, CZO@C and CZO@C/CNT were showed in Figure 3c, d and e, respectively. In these figures, two broad peaks at 1333.3 and 1581.1 cm^{-1} were obviously observed, which could be marked as the D and G bands of carbon, respectively. [32] The I_D/I_G ratio of ZnO@C, CZO@C and CZO@C/CNT was 1.65, 1.40 and 1.05, respectively. The doped Co enhanced the graphitization degree of the carbon during the calcining process, [30]

which resulted in a lower I_D/I_G ratio of CZO@C than ZnO@C. The lowest I_D/I_G ratio was 1.05 , which was attributed to the in situ formed CNTs in CZO@C/CNT.

In the C 1s core level XPS spectrum (Figure 4a and b), the peaks at 284.5 eV, 285.3 eV, 286.7 eV and 289.0 eV belonged to the bonds of C-C, [33] C=C, [34] C-O [35] and O-C=O, [35] respectively. The increased relative intensity of the peak at 285.3 eV confirmed that most carbon atoms were sp^2 hybridization in CZO@C/CNT, which was in accordance with the Raman shift. Two peaks at 781.1 eV for Co $2p_{3/2}$ and 796.8 eV for Co $2p_{1/2}$ were observed in Figure 4c and d. The energy difference was 15.4 eV, which showed that the major existence state of Co element was Co (II) oxidation state. [36] Moreover, the burr of the curve was caused by the low content of Co in the composites. The peaks at 786.8 and 802.5 eV were ascribed to the satellite peaks. The binding energies of Zn $2p_{3/2}$ peak and Zn $2p_{1/2}$ peak of ZnO@C were at 1020.7 eV and 1043.8 eV, indicating that the existence state of the Zn element was Zn (II) oxidation state [37] (Figure S5a). However, the relative peaks of CZO@C and CZO@C/CNT were a little positive shift to bonding energy (Figure S5b and c) which was caused by the Co doping. The result was in accordance with the XRD patterns.

N_2 adsorption-desorption measurement has been taken to characterize the specific surface areas and pore size distribution of CZO@C/CNT. As shown in Figure S6a, a type IV isotherm with an unconspicuous hysteresis loop in middle pressure region occurs, indicated the mesoporous characteristics. The Brunauer-Emmett-Teller (BET) surface areas and total pore volume of CZO@C/CNT were 102.8 $m^2\ g^{-1}$ and 0.31 $cm^3\ g^{-1}$, respectively. The poresize distribution calculated from the Barrett-Joyner-Halenda (BJH) method showed that the CZO@C/CNT were mesoporous composites with a wide distribution centered at 40 nm, and also some macropores (Figure S6b).

The initial discharge capacities of CZO@C/CNT, CZO@C and ZnO@C composites were 1551, 880 and 903 mA h g^{-1}, respectively (Fig.5a, b and c). These characters became 1091, 640 and 665 mA h g^{-1} at the second cycle. The charge and discharge capacity of CZO@C/CNT at 10^{th} cycle were almost same with the values at 50^{th} cycle, which showed the best stability of CZO@C/CNT composites. These high irreversible capacities at the first cycle were caused by the formation of solid electrolyte interphase (SEI) layer on the surface of the electrode. [29, 38] The capacity decay was quite large at the first five cycles. One reason was the morphological change during the formation of the Li_xZn alloys and the other was the poor conductivity of ZnO. [39] The CZO@C/CNT composites exhibited an enhanced electrochemical performance compared with ZnO@C and CZO@C composites (Figure 5d). The CZO@C/CNT composites had a high discharge capacity of 758 mA h g^{-1} after 100 cycles, which was much higher than that of CZO@C (523 mA h g^{-1} after 100 cycles) and ZnO@C (335 mA h g^{-1} after 50 cycles). The promoted performance of CZO@C/CNT compared with CZO@C was attributed to the CNTs in the composites. The conductive network was formed and the conductivity of the material was enhanced, which was beneficial to the easier electron transfer in the material. The reactions of CZO with Li were similar to that of ZnO, including the reversible conversion metal oxide to nanosized metal and Li oxide matrix, the alloying and dealloying processes of metal and Li[40, 41]. The reactions were as follows:

Discharge process:

$$CZO + 2Li^+ + 2e^- \rightarrow Zn + Co + Li_2O \quad (1)$$

$$Zn + Li^+ + e^- \rightarrow LiZn \quad (2)$$

$$Co + Li^+ + e^- \rightarrow LiCo \quad (3)$$

Charge process:

$$LiZn \rightarrow Zn + Li^{+} + e^{-} \quad (4)$$

$$LiCo \rightarrow Co + Li^{+} + e^{-} \quad (5)$$

$$Zn + Li_2O \rightarrow ZnO + 2Li^{+} + 2e^{-} \quad (6)$$

$$Co + Li_2O \rightarrow CoO + 2Li^{+} + 2e^{-} \quad (7)$$

The EIS experiments were carried out (Figure 5e) to further understand the improved Li storage performance of the CZO@C/CNT composites. All of the Nyquist plots showed depressed separate semicircles in the middle and high frequency region and a straight line in the low frequency region. The semicircles were corresponded to charge-transfer resistances to Li ions at the interface between the electrode and electrolyte (R_p) and the electronic resistivity of the active material and ionic conductivity in the electrode (R_b) .[12, 13] The straight line was assigned to the Warburg impedance (W_o) corresponding to the Li diffusion process,[42] and R_s represented the internal resistance of the test battery. As shown in Figure 5e, CZO based composites showed a distinctly smaller semicircle, indicating that they had lower charge-transfer impedances and electronic resistivity than that of ZnO@C compositesowing to that Co doping could enhance the conductivity of ZnO. The tiny conduction promotion of CZO@C/CNT was attributed to the CNTs in the composite.

Finally, the capacities presented in this work were compared with those taken from the literature for various electrodes made from ZnO based anode materials, as shown in Table 1:

4. CONCLUSIONS

The CNTs was in situ grew out in CZO@C/CNT during the calcination of Co-MOF-105 at 600 °C. The catalyst was metal Co and the carbon source was terephthalic acid, which played as organic linker in MOF. Moreover, the sp^2 hybridization which carbon atoms were in terephthalic acid decreased the energy barrier during the CNTs growth. The TEM and SEM observation

found that the CNTs were interspersed in the material and connected the CZO@C nanoparticles together. The other advantages of Co doping were enhancing the conductivity of ZnO and increasing the graphitization degree of the carbon on the surface of CZO@C nanoparticles. All of the three advantages of Co doping made the electron transfer easier in the material. When the CZO@C/CNT composite was used as anode material for LIBs, an enhanced electrochemical performance of 758 mA h g^{-1} after 100 cycles at the current density of 100 mA g^{-1} was obtained.

Acknowledgment

This work was financially supported by Research Fund for the Doctoral Program of Higher Education of China (No. qd12124), Major Science and Technology Projects in Henan Province (No. 121100210500) and Key Project of Science and Technology of Henan Educational Committee (No. 13A150518).

References

1. J. B. Goodenough and K. S. Park, *J. Am. Chem. Soc.*, 2013, **135**, 1167-1176.
2. G. Girishkumar, B. McCloskey, A. C. Luntz, S. Swanson and W. Wilcke, *J. Phys. Chem. Lett.*, 2010, **1**, 2193-2203.
3. K. Amine, R. Kanno and Y. H. Tzeng, *MRS Bull.*, 2014, **39**, 395-405.
4. A. Manthiram, Y. Fu, S. H. Chung, C. Zu and Y. S. Su, *Chem. Rev.*, 2014, **114**, 11751-11787.
5. M. V. Reddy, G. V. Subba Rao and B. V. Chowdari, *Chem. Rev.*, 2013, **113**, 53645-53457.
6. A. D. Roberts, X. Li and H. Zhang, *Chem. Soc. Rev.*, 2014, **43**, 4341-4356.
7. P. Roy and S. K. Srivastava, *J. Mater. Chem. A*, 2015, **3**, 2454-2484.
8. G. Z. Yang, H. W. Song, H. Cui, Y. C. Liu and C. X. Wang, *Nano Energy*, 2013, **2**, 579-585.

9. J. Xie, N. Imanishi, A. Hirano, Y. Takeda, O. Yamamoto, X. B. Zhao and G. S. Cao, *Thin Solid Films*, 2011, **519**, 3373-3377.

10. V. Aruoja, H. C. Dubourguier, K. Kasemets and A. Kahru, *Sci. Total. Environ.*, 2009, **407**, 1461-1468.

11. X. Sun, C. G. Zhou, M. Xie, H. T. Sun, T. Hu, F. Y. Lu, S. M. Scott, S. M. George and J. Lian, *J. Mater. Chem. A*, 2014, **2**, 7319-7326.

12. C. T. Hsieh, C. Y. Lin, Y. F. Chen and J. S. Lin, *Electrochim. Acta*, 2013, **111**, 359-365.

13. Z. M. Ren, Z. Y. Wang, C. Chen, J. Wang, X. X. Fu, C. Y. Fan and G. D. Qian, *Electrochim. Acta*, 2014, **146**, 52-59.

14. Y. Hwa, J. H. Sung, B. Wang, C. M. Park and H. J. Sohn, *J. Mater. Chem.*, 2012, **22**, 12767-12773.

15. Q. Xie, Y. Ma, D. Zeng, X. Zhang, L. Wang, G. Yue and D. L. Peng, *ACS Appl. Mater. Interfaces*, 2014, **6**, 19895-19904.

16. L. J. Liu, C. Y. Zhao, H. L. Zhao, Q. Y. Zhang and Y. Li, *Electrochim. Acta*, 2014, **135**, 224-231.

17. R. Guo, W. B. Yue, Y. M. An, Y. Ren and X. Yan, *Electrochim. Acta*, 2014, **135**, 161-167.

18. S. M. Abbas, S. T. Hussain, S. Ali, N. Ahmad, N. Ali and S. Abbas, *J. Mater. Sci.*, 2013, **48**, 5429-5436.

19. S. L. Li and Q. Xu, *Energy Environ. Sci.*, 2013, **6**, 1656-1683.

20. W. Xuan, C. Zhu, Y. Liu and Y. Cui, *Chem. Soc. Rev.*, 2012, **41**, 1677-1695.

21. T. A. Makal, J. R. Li, W. Lu and H. C. Zhou, *Chem. Soc. Rev.*, 2012, **41**, 7761-7779.

22. H. L. Jiang, Y. Tatsu, Z. H. Lu and Q. Xu, *J. Am. Chem. Soc.*, 2010, **132**, 5586-5587.

23. J. Lee, O. K. Farha, J. Roberts, K. A. Scheidt, S. T. Nguyen and J. T. Hupp, *Chem. Soc.*

Rev., 2009, **38**, 1450-1459.

24. L. Yang, S. Kinoshita, T. Yamada, S. Kanda, H. Kitagawa, M. Tokunaga, T. Ishimoto, T. Ogura, R. Nagumo, A. Miyamoto and M. Koyama, *Angew. Chem. Int. Ed.*, 2010, **49**, 5348-5351.

25. W. Yin, Y. Shen, F. Zou, X. Hu, B. Chi and Y. Huang, *ACS Appl. Mater. Interfaces*, 2015, **7**, 4947-4954.

26. F. Zou, X. Hu, Z. Li, L. Qie, C. Hu, R. Zeng, Y. Jiang and Y. Huang, *Adv. Mater.*, 2014, **26**, 6622-6628.

27. D. K. Lee, J. H. Park, J. I. Choi, Y. Lee, S. J. Kim, G. H. Lee, Y. H. Kim and J. K. Kang, *Nanoscale*, 2014, **6**, 10995-11001.

28. S. J. Yang, S. Nam, T. Kim, J. H. Im, H. Jung, J. H. Kang, S. Wi, B. Park and C. R. Park, *J. Am. Chem. Soc.*, 2013, **135**, 7394-7397.

29. G. Zhang, S. Hou, H. Zhang, W. Zeng, F. Yan, C. C. Li and H. Duan, *Adv. Mater.*, 2015, **27**, 2400-2405.

30. H. Y. Yue, Z. P. Shi, Q. X. Wang, Z. X. Cao, H. Y. Dong, Y. Qiao, Y. H. Yin and S. T. Yang, *ACS Appl. Mater. Interfaces*, 2014, **6**, 17067-17074.

31. J. Hafizovic, M. Bjorgen, U. Olsbye, P. D. C. Dietzel, S. Bordiga, C. Prestipino, C. Lamberti and K. P. Lillerud, *J. Am. Chem. Soc.*, 2007, **129**, 3612-3620.

32. Z. Q. Zhu, S. W. Wang, J. Du, Q. Jin, T. R. Zhang, F. Y. Cheng and J. Chen, *Nano Lett.*, 2014, **14**, 153-157.

33. Y. Liu, W. Wang, L. Gu, Y. W. Wang, Y. L. Ying, Y. Y. Mao, L. W. Sun and X. S. Peng, *ACS Appl. Mater. Interfaces*, 2013, **5**, 9850-9855.

34. A. J. Maxwell, P. A. Brühwiler, A. Nilsson, N. Mårtensson and P. Rudolf, *Physical*

Review B, 1994, **49**, 10717-10725.

35. H. L. Poh, P. Simek, Z. Sofer and M. Pumera, *ACS Nano*, 2013, **7**, 5262-5272.

36. S. Y. Yang, R. Q. Lv, C. Z. Wang, Y. Y. Liu and Z. Q. Song, *J. Alloys Compd.*, 2013, **579**, 628-632.

37. T. F. Hung, S. G. Mohamed, C. C. Shen, Y. Q. Tsai, W. S. Chang and R. S. Liu, *Nanoscale*, 2013, **5**, 12115-12119.

38. X. Shen, D. Mu, S. Chen, B. Wu and F. Wu, *ACS Appl. Mater. Interfaces*, 2013, **5**, 3118-3125.

39. C. Q. Zhang, J. P. Tu, Y. F. Yuan, X. H. Huang, X. T. Chen and F. Mao, *J. Electrochem. Soc.*, 2007, **154**, A65-A69.

40. H. Q. Dai, H. Xu, Y. N. Zhou, F. Lu and Z. W. Fu, *J. Phys. Chem. C*, 2012, **116**, 1519-1525.

41. L. L. Hu, B. H. Qu, C. C. Li, Y. J. Chen, L. Mei, D. N. Lei, L. B. Chen, Q. H. Li and T. H. Wang, *J. Mater. Chem. A*, 2013, **1**, 5596-5602.

42. L. Chen, H. Y. Xu, L. Li, F. F. Wu, J. Yang and Y. T. Qian, *J. Power Sources*, 2014, **245**, 429-435.

43. K. T. Park, F. Xia, S. W. Kim, S. B. Kim, T. Song, U. Paik and W. I. Park, *J. Phys. Chem. C*, 2013, **117**, 1037-1043.

Table 1. Comparison of cycling performance among ZnO based anode materials

electrode material	reversible capacity (mA h g^{-1})	cycle number	voltage (V)	Rate (mA g^{-1})	Ref.
Ultrathin ZnO Nanotubes	386	50	0.01-2.5	494	43
ZnO/$ZnCo_2O_4$ rods	900	30	0.01-3.0	45	41
Ni-coated ZnO	490	30	0.02-3.0	80	39
ZnO−Ag−C	729	200	0.01-3.0	100	15
ZnO@C-5	518	300	0.02-3.0	110	13
G-C8-ZnO[a]	560	100	0.01-3	97.8	17
ZnO@ZnO QDs/C NRAs	699	100	0.01-2	500	29
ZnO-M/PC	653	100	0.1-3.0	100	38
CZO@C	523	100	0.01-3.0	100	This work
CZO@C/CNT	758	100	0.01-3.0	100	This work

[a] graphene-encapsulated porous carbon-ZnO

Figure Captions:

Figure 1. TEM (a and b) and HRTEM (c, d, e and f) images of CZO@C/CNTs.

Figure 2. SEM images of Co-MOF-120 (a), Co-MOF-105 (b), CZO@C (c) and CZO@C/CNT (d).

Figure 3. XRD patterns of the as synthesized MOFs (a) and ZnO based materials (b); Raman shift of as synthesized ZnO@C (c), CZO@C (d) and CZO@C/CNT (e).

Figure 4. C 1s core level XPS profiles spectra of CZO@C (a) and CZO@C/CNT (b); Co 2p core level XPS profiles spectra of CZO@C (c) and CZO@C/CNT (d).

Figure 5. Charge/discharge curve of ZnO@C (a), CZO@C (b), CZO@C/CNT (c), cycling performance (d) and Nyquist plots of the three ZnO based materials after 50 cycles (e).

Figure 1

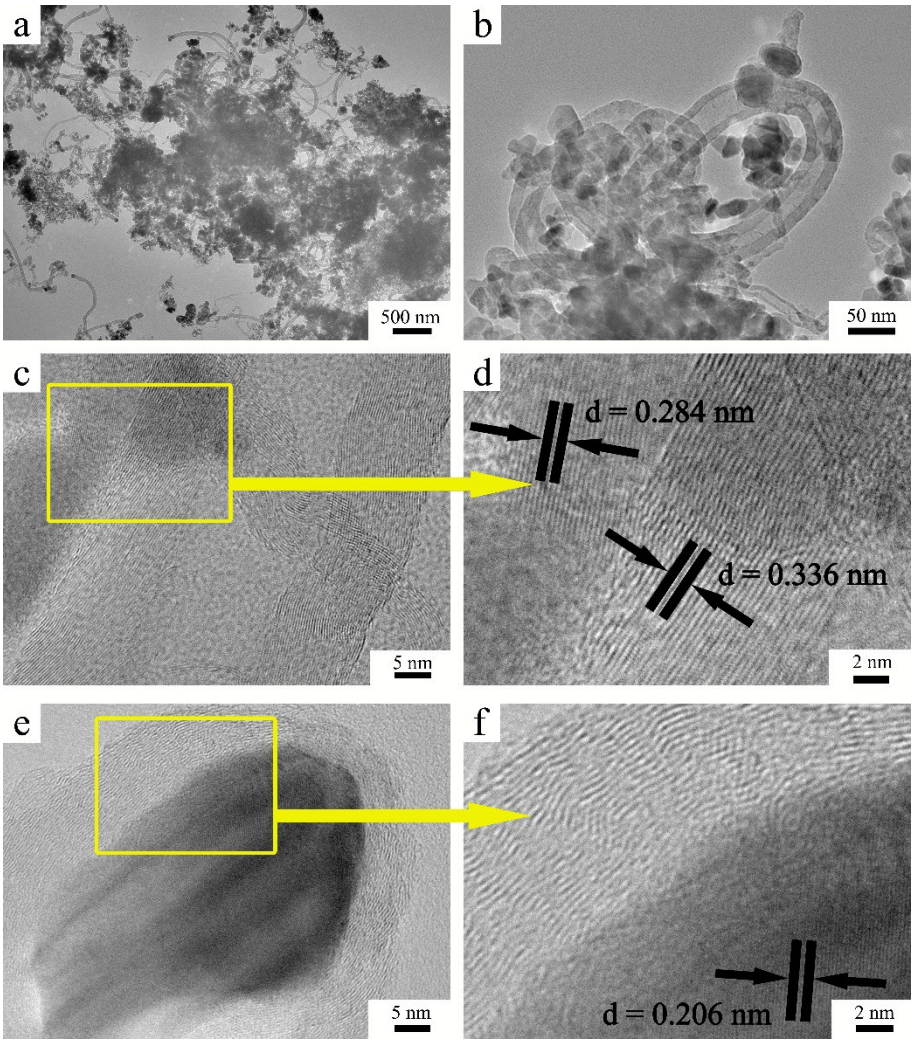

Figure 1. TEM (a and b) and HRTEM (c, d, e and f) images of CZO@C/CNTs.

Figure 2

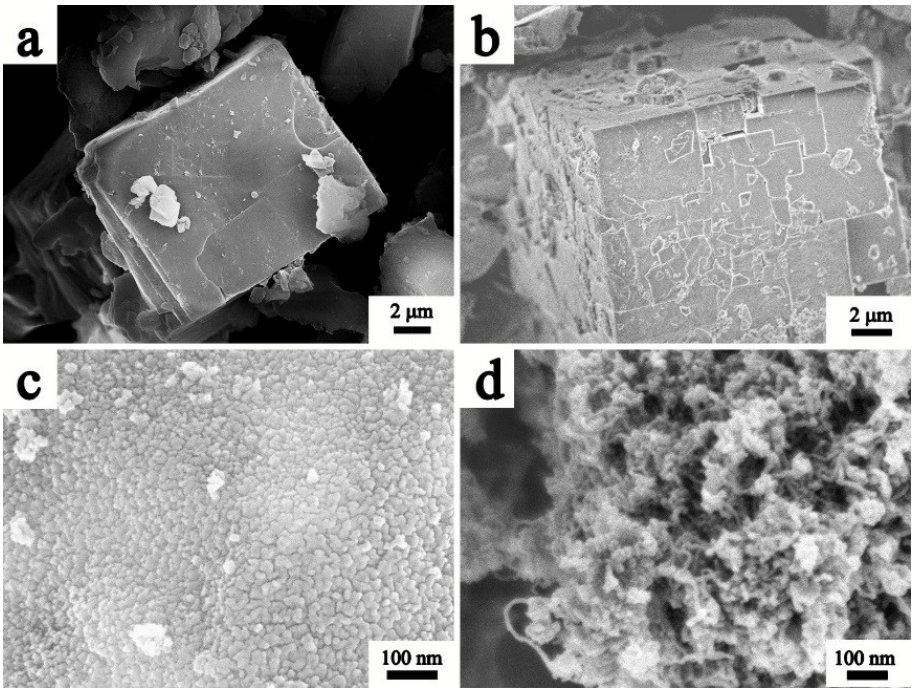

Figure 2. SEM images of Co-MOF-120 (a), Co-MOF-105 (b), CZO@C (c) and CZO@C/CNT (d).

Figure 3

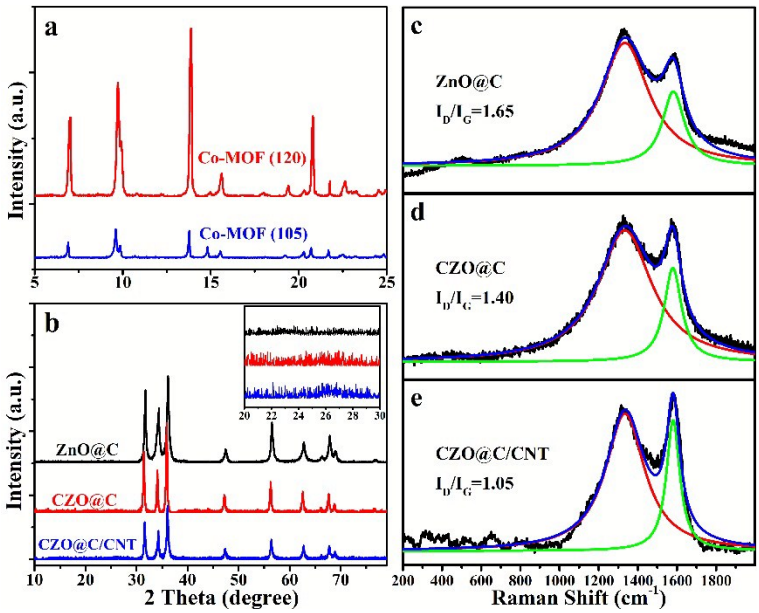

Figure 3. XRD patterns of the as synthesized MOFs (a) and ZnO based materials (b); Raman shift of as synthesized ZnO@C (c), CZO@C (d) and CZO@C/CNT (e).

Figure 4

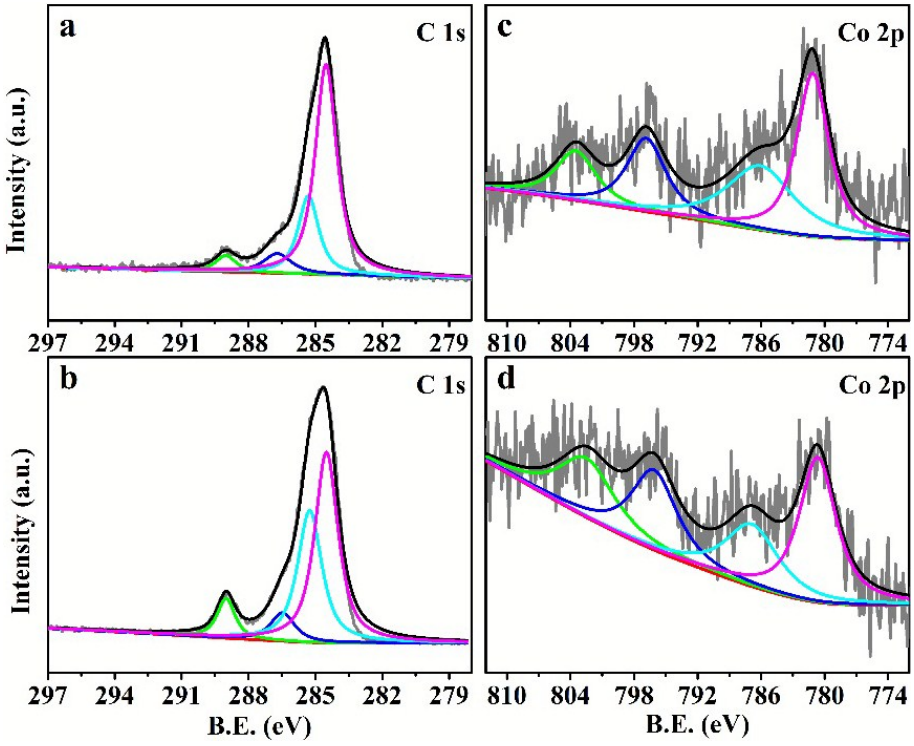

Figure 4. C 1s core level XPS profiles spectra of CZO@C (a) and CZO@C/CNT (b); Co 2p core level XPS profiles spectra of CZO@C (c) and CZO@C/CNT (d).

Figure 5

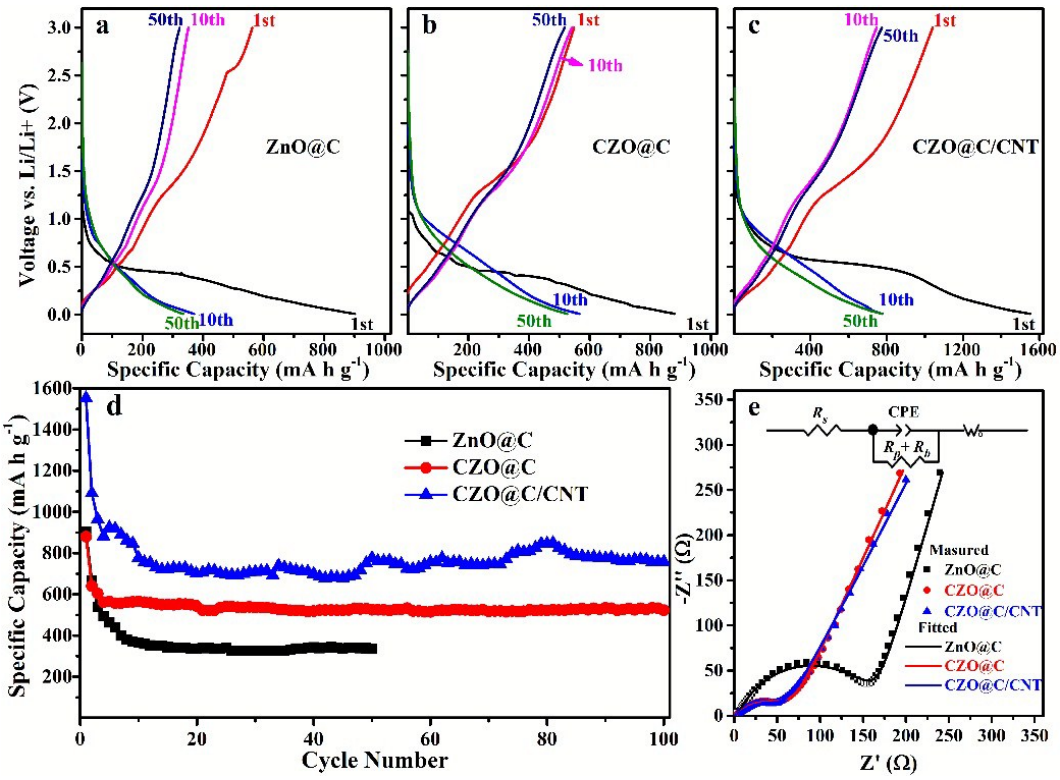

Figure 5. Charge/discharge curve of ZnO@C (a), CZO@C (b), CZO@C/CNT (c), cycling performance (d) and Nyquist plots of the three ZnO based materials after 50 cycles (e).

Graphic Abstract